Article

Highly structured slow solar wind emerging from an equatorial coronal hole

https://doi.org/10.1038/s41586-019-1818-7

Received: 16 July 2019

Accepted: 11 November 2019

Published online: 4 December 2019

S. D. Bale[1,2,3,4]*, S. T. Badman[1,2], J. W. Bonnell[1], T. A. Bowen[1], D. Burgess[4], A. W. Case[5], C. A. Cattell[6], B. D. G. Chandran[7,8], C. C. Chaston[1], C. H. K. Chen[4], J. F. Drake[9,10,11], T. Dudok de Wit[12], J. P. Eastwood[3], R. E. Ergun[13], W. M. Farrell[14], C. Fong[1,2], K. Goetz[6], M. Goldstein[15,16], K. A. Goodrich[1], P. R. Harvey[1], T. S. Horbury[3], G. G. Howes[17], J. C. Kasper[5,18], P. J. Kellogg[6], J. A. Klimchuk[19], K. E. Korreck[5], V. V. Krasnoselskikh[12], S. Krucker[1,20], R. Laker[3], D. E. Larson[1], R. J. MacDowall[14], M. Maksimovic[21], D. M. Malaspina[13], J. Martinez-Oliveros[1], D. J. McComas[22], N. Meyer-Vernet[21], M. Moncuquet[21], F. S. Mozer[1], T. D. Phan[1], M. Pulupa[1], N. E. Raouafi[23], C. Salem[1], D. Stansby[3], M. Stevens[5], A. Szabo[19], M. Velli[24], T. Woolley[3] & J. R. Wygant[6]

During the solar minimum, when the Sun is at its least active, the solar wind[1,2] is observed at high latitudes as a predominantly fast (more than 500 kilometres per second), highly Alfvénic rarefied stream of plasma originating from deep within coronal holes. Closer to the ecliptic plane, the solar wind is interspersed with a more variable slow wind[3] of less than 500 kilometres per second. The precise origins of the slow wind streams are less certain[4]; theories and observations suggest that they may originate at the tips of helmet streamers[5,6], from interchange reconnection near coronal hole boundaries[7,8], or within coronal holes with highly diverging magnetic fields[9,10]. The heating mechanism required to drive the solar wind is also unresolved, although candidate mechanisms include Alfvén-wave turbulence[11,12], heating by reconnection in nanoflares[13], ion cyclotron wave heating[14] and acceleration by thermal gradients[1]. At a distance of one astronomical unit, the wind is mixed and evolved, and therefore much of the diagnostic structure of these sources and processes has been lost. Here we present observations from the Parker Solar Probe[15] at 36 to 54 solar radii that show evidence of slow Alfvénic solar wind emerging from a small equatorial coronal hole. The measured magnetic field exhibits patches of large, intermittent reversals that are associated with jets of plasma and enhanced Poynting flux and that are interspersed in a smoother and less turbulent flow with a near-radial magnetic field. Furthermore, plasma-wave measurements suggest the existence of electron and ion velocity-space micro-instabilities[10,16] that are associated with plasma heating and thermalization processes. Our measurements suggest that there is an impulsive mechanism associated with solar-wind energization and that micro-instabilities play a part in heating, and we provide evidence that low-latitude coronal holes are a key source of the slow solar wind.

The first solar encounter of the Parker Solar Probe (PSP) occurred during the solar minimum. The spacecraft orbit remained within 5° of the heliographic solar equator and, unlike any previous spacecraft, was corotational with the Sun for two intervals surrounding perihelion. Figure 1 summarizes the radial magnetic field (B_R; in heliocentric RTN coordinates; see Methods) structure observed by the FIELDS experiment[17] for a six-week time interval centred on perihelion (6 November 2018). Figure 1a shows 1-s cadence measurements of B_R (see Methods) which show the overall $1/r^2$ behaviour expected from simple flux-conservation arguments[18] as the heliocentric distance of PSP varied along its eccentric orbit. Against this background, dramatic and unexpected rapid polarity reversals where $\delta B_R/|\mathbf{B}|$ is of the order of 1 are superposed ($|\mathbf{B}|$ is the magnitude of the magnetic field). One-hour statistical modes (most probable value; see Methods) of B_R in Fig. 1b remove the transient polarity inversions and reveal the large-scale magnetic structure. Time series predictions of B_R generated from the simple, but widely used, Potential Field Source Surface (PFSS) model[19–21] are shown for comparison in black and green. The implementation of this model and the procedure to connect it to the location of PSP and generate the time series is discussed in the Methods section 'PFSS modelling and connection to PSP'.

Magnetic field structure

PFSS is a zero-current force-free model of the global solar corona, meaning that it assumes that magnetic pressure dominates over gas

The list of affiliations appears at the end of the paper.

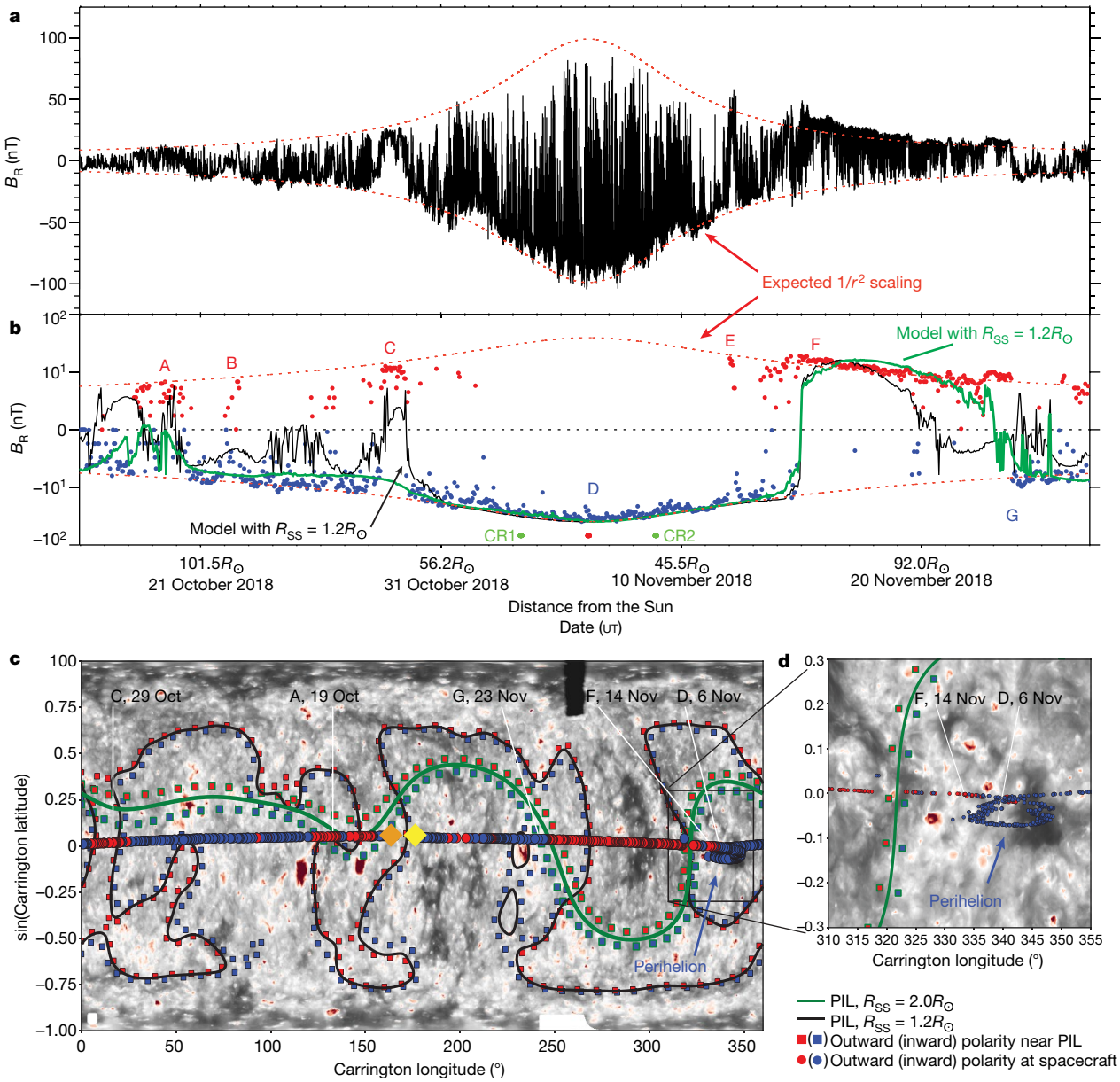

Fig. 1 | Radial magnetic field measurements are highly structured, map back to the Sun, and are consistent with a low source surface. a, The measured radial magnetic field B_R is comprised of a large-scale field, which scales approximately as $1/r^2$ (red dotted lines; also in Fig. 1b) and rapid large-amplitude polarity reversals ($\delta B_R/|\mathbf{B}|$ of the order of 1) associated with jets of plasma (Fig. 2b). **b**, One-hour statistical modes of B_R (bisymmetric logarithmic plot) show the large-scale radial field coloured for polarity (red, outward; blue, inward). Predicted radial-field profiles from a PFSS model are over-plotted using a source-surface radius of $R_{SS} = 1.2R_\odot$ (black curve, unscaled) and $2.0R_\odot$ (green curve, multiplied by a factor of 6.5). R_{SS} at $1.2R_\odot$ reproduces many of the measured polarity changes (labelled A, C, F and G). The $R_{SS} = 2.0R_\odot$ model better predicts the timing of polarity inversion G (see Methods). Labels B and E indicate transient events, and the perihelion coronal hole interval is centred on D. Corotations (CR1 and CR2; green) and the perihelion (PH; red dot) at $35.7R_\odot$ are labelled. **c**, An extreme-ultraviolet synoptic map of 171-Å (Fe IX) emission shows structure associated with active regions (small-scale extreme-ultraviolet bright points appear as red patches) and lower-density plasma in coronal holes (darker regions). The PSP trajectory at the source surface is superimposed, coloured as in **b** for measured field polarity. Encounter 1 begins at the orange diamond, moves westwards (in decreasing Carrington longitude, with respect to a fixed point on the solar surface) across the map through perihelion at about 330°, and ends at the yellow diamond. A line shows the location of the model polarity-inversion line (PIL) at the source surface ($R_{SS} = 1.2R_\odot$, black; $R_{SS} = 2.0R_\odot$, green). Red and blue squares indicate the polarity on either side of the PIL models. Red ($B_R > 0$) and blue ($B_R < 0$) lines map the magnetic field from R_{SS} back to the photosphere for $R_{SS} = 2.0R_\odot$; for $R_{SS} = 1.2R_\odot$ the model field lines are radial. **d**, The extreme-ultraviolet map of the perihelion interval, showing field lines mapping back to the Sun into a small equatorial coronal hole, and the location of the adjacent PIL associated with the heliospheric current sheet, from the $2.0R_\odot$ model.

pressure (that is, it assumes a low plasma β value), so that the problem reduces to magnetostatics, giving a solution of a static field configuration that rigidly corotates with the Sun. The role of gas dynamics is approximated by requiring that the tangential magnetic field vanishes at a spherical 'source surface' at some radius R_{SS}, which simulates how the outflowing solar wind drags the field lines out into the heliosphere. The magnetostatic approximation limits the accuracy and applicability of the model. Nevertheless, PFSS is widely used as a computationally tractable first approximation and forms the basis for more sophisticated models[21,22]. We note that PSP encounter 1 took place very close to solar minimum, with low solar activity, reducing the impact of non-potential transient events and active regions.

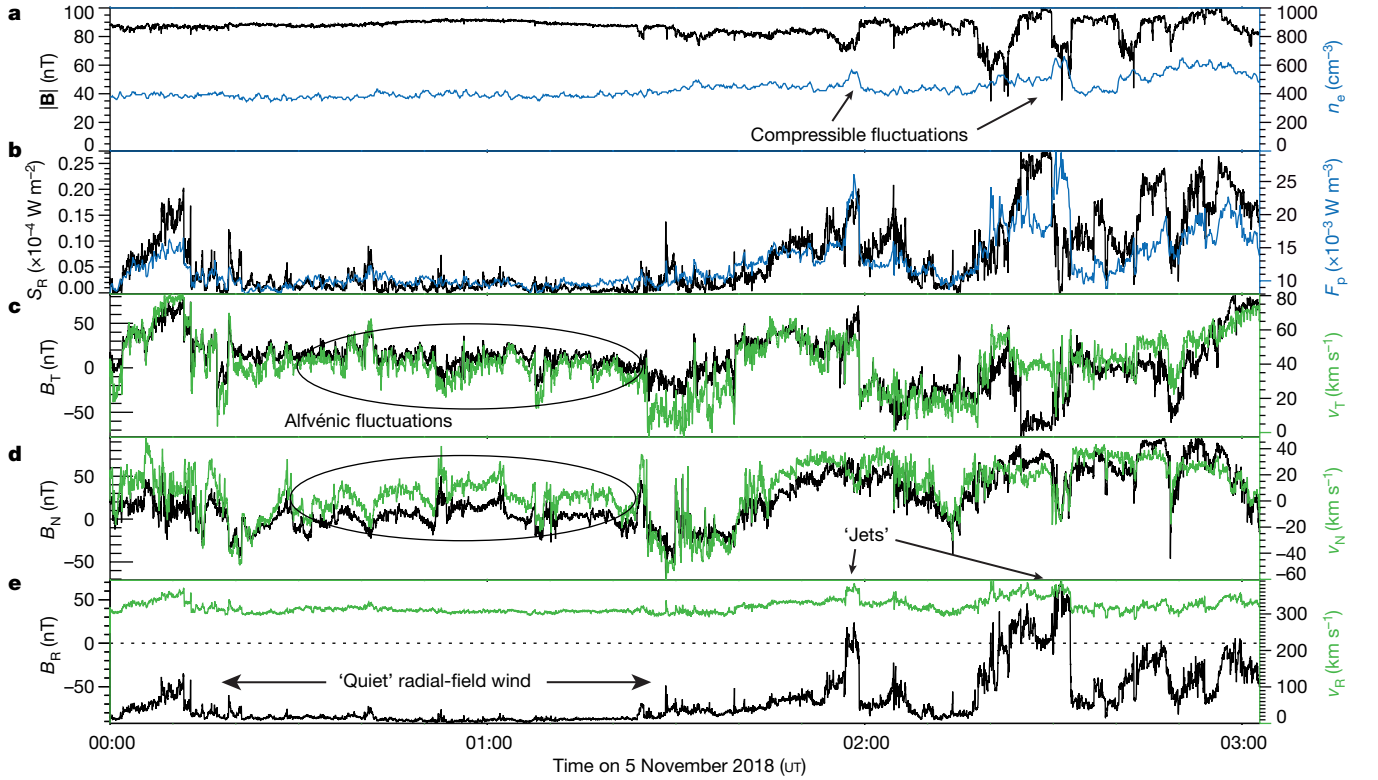

Fig. 2 | Magnetic field reversals and plasma jets carry a Poynting flux. a, Time series measurements of the magnetic field magnitude |**B**| (black line) and total plasma density n_e (blue line) show anti-correlation during jet events, consistent with magnetohydrodynamic slow-mode behaviour. **b**, Radial Poynting flux (S_R, black line) and ion kinetic energy flux (F_p, blue line), showing large enhancements during jet–field reversal events. **c**, Tangential components of the magnetic field (B_T; black) and plasma velocity (v_T, green) components showing Alfvénic fluctuations. **d**, The normal components of the magnetic field (B_N, black line) and the plasma velocity (v_N, green line). **e**, Radial magnetic field (B_R, black line) and plasma velocity (v_R, green line), showing an interval of quiet radial-field wind and flow adjacent to a magnetic structure associated with jets of plasma. Measurements are made from around 00:00 to 03:00 5 November 5 2018 universal time (UT) at about 36.6$R_\odot$. The Alfvén speed during the quiet interval is $v_A \approx 100$ km s^{-1}.

In Fig. 1b, two model evaluations are shown with $R_{SS} = 2.0R_\odot$ ($R_\odot$, solar radius; green line) and $R_{SS} = 1.2R_\odot$ (black line). In both cases R_{SS} is well below the established value[23]. However, this value is necessary to provide good agreement for all model inputs (see Methods) and is not without precedent[24,25]. Model comparison reveals an overall very good agreement for both models, but also shows that the polarity inversions at features A and C are washed out except with the lower source-surface radius (black line). Meanwhile, the timing of feature G is better captured with the higher source-surface radius (green line), illustrating the difficulty that PFSS has with assuming a single source-surface radius, and supports previous findings of a varying 'true' source-surface radius[25,26]. Finally, Fig. 1c, d depicts field-line mappings derived from the same PFSS models shown in Fig. 1b to connect the spacecraft down to the lower corona to establish context for the in situ measurements. The spacecraft trajectory is shown projected onto the source surface, coloured by its measured polarity.

The background is a synoptic map of extreme-ultraviolet emission in the 171-Å wavelength for which dark regions imply lower-density plasma and the likely location of open magnetic field lines. For reference, this background is shown in isolation in Extended Data Fig. 4 along with its corresponding map for the 193-Å wavelength. The neutral lines derived from the PFSS models are shown as single contours in the same colour as their time series in Fig. 1b. Figure 1c shows how the neutral line topology explains the polarity inversions measured by PSP. Figure 1d is a magnification of the two-week interval closest to perihelion (330° longitude). During the entire two-week corotation loop period, PSP remained connected to a small, negative-polarity, isolated equatorial coronal hole, suggesting that the rapid magnetic field polarity reversals seen in Fig. 1a are magnetic structures emerging from this coronal hole and sweeping past the PSP spacecraft. Extended Data Fig. 5 shows the configuration schematically. For most of this interval, SWEAP[27] measurements of the solar-wind velocity indicated an Alfvénic slow wind stream (see Fig. 2), suggesting a slow solar wind source rooted in an equatorial coronal hole at the Sun. Polarity inversions B and E in Fig. 1b are associated with (transient) flux rope and coronal mass ejection[28] events, respectively.

Alfvenic fluctuations and plasma jets

Time series magnetic field and velocity structures show the correlations (Fig. 2c–e) expected of propagating Alfvén waves[29], especially during the quiet radial-field intervals. The δB_R polarity reversal intervals show enhanced radial wind velocity v_R (Fig. 2e) and the Alfvénic correlations of velocity and magnetic field ($\delta\mathbf{v}$ to $\delta\mathbf{B}$) within the polarity inversions and jets suggest that these structures may be interpreted as large-amplitude, three-dimensional Alfvénic structures convected away from the Sun. As a simple measure, statistics of zero-crossings (polarity reversals; see Methods) show that around 6% of the temporal duration of encounter 1 is comprised of these so-defined jets. Many jet intervals show signatures of compressibility (Fig. 2a)—in this case anti-correlated plasma density n_e and |**B**|—suggesting slow-mode or pressure-balanced behaviour[30]. Isolated Alfvénic features associated with magnetic field reversals have been identified at 60$R_\odot$ (ref. [31]), near one astronomical unit (AU)[32] and in the polar heliosphere by the spacecraft Ulysses[33]; however, at those distances few or no compressive signatures were present. It has been suggested[34] that these magnetic structures could be signatures of impulsive reconnection events in the Sun's atmosphere[35]; simulations[36] show qualitative similarities to the events of encounter 1 but do not reproduce the observed magnetic field reversals past 90°.

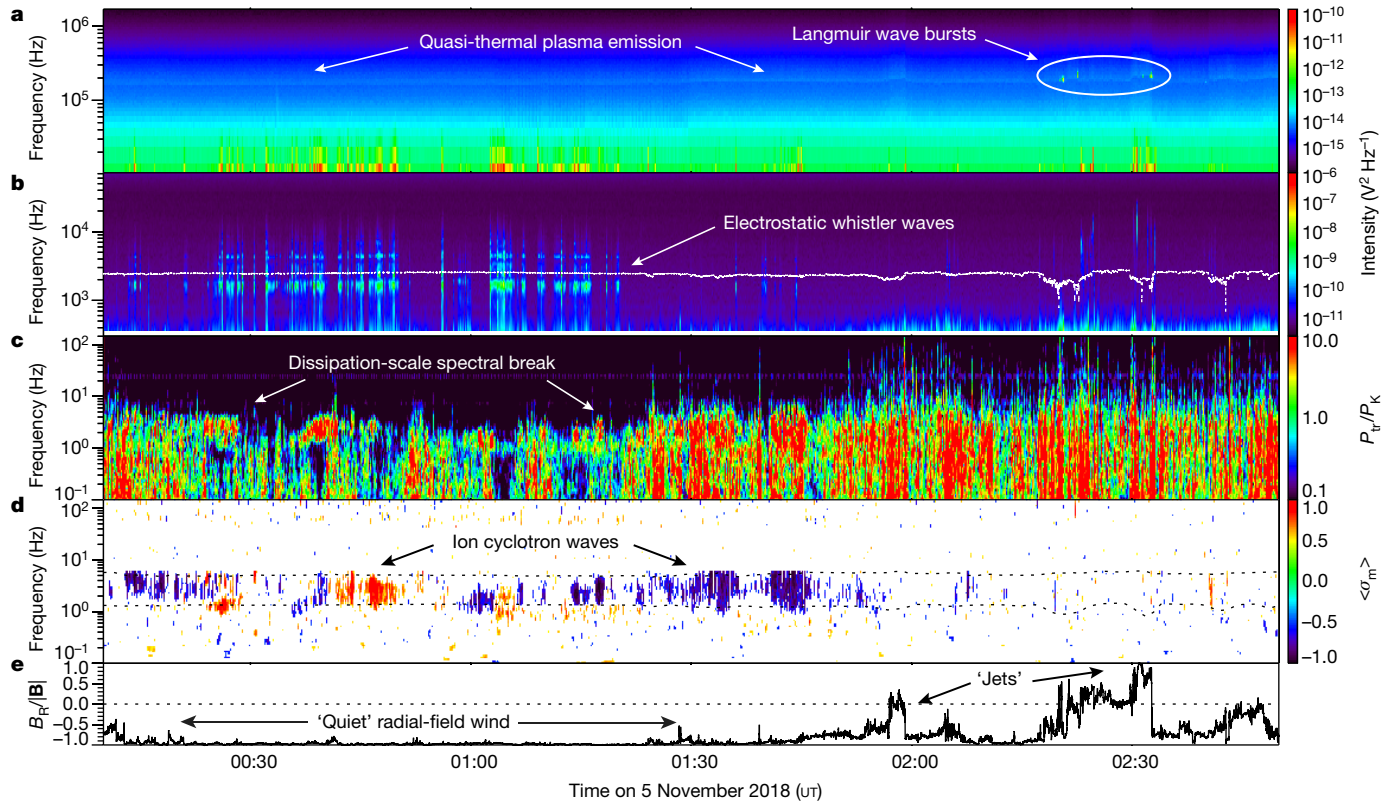

Fig. 3 | Plasma-wave activity near the perihelion differs in quiet wind and jets. a, Spectral density measurements of electric field fluctuations near the electron plasma frequency f_{pe} show intense bursts of electrostatic Langmuir waves with intensities around 10^2–10^4 $V^2 Hz^{-1}$ above the thermal background, suggesting the presence of electron beams. **b**, Electrostatic waves near the electron cyclotron frequency f_{ce} (white dotted line) and its harmonics are often present in intervals of ambient radial magnetic field, but not present in jet plasma. **c**, A wavelet spectrogram of the magnetic field shows bursts of turbulent fluctuations with a distinct spectral break between 1 and 10 Hz associated with a transition to dissipation scales. The trace magnetic field intensity (P_{tr}) is divided by a factor of $P_K \propto f^{-5/3}$ such that a power spectrum with index −5/3 has no frequency dependence. **d**, Magnetic helicity (σ_m, from the wavelet spectrogram) shows narrowband $f_{ci} < f < f_{ci} + v_R/v_A$ (the expected Doppler-shifted frequency, where v_A is the local Alfvén speed; dashed lines) signatures associated with ion cyclotron waves—when σ_m is close to the maximum (+1) or the minimum (−1)—again in quiet radial solar wind. **e**, The normalized radial magnetic field $B_R/|B|$ shows distinct intervals of quiet radial-field wind, reduced turbulent levels and increased occurrence of electrostatic whistler and ion cyclotron instability. Measurements in Fig. 3 were made at approximately 00:00–03:00 November 5 2018 UT at about $36.6R_\odot$.

Alfvénic structures and waves have long been considered to be an important energy source for the solar wind[11,12]. The radial Poynting flux $S_R = (\mathbf{E} \times \mathbf{B})_R/\mu_0$ (where μ_0 is the vacuum permeability and $\mathbf{E}$ is the electric field; see Methods) in the spacecraft frame (Fig. 2b) is about 10% of the kinetic energy flux (blue curve) and shows enhancements during the jet intervals, suggesting that these plasma jets may impart energy to the emerging solar wind. As seen in Figs. 1a, 2e, the plasma jets appear to be clustered and interspersed in an otherwise quiet solar wind flow with prominently radial magnetic field.

Micro-instabilities and turbulence

The quiet radial-flow intervals contain plasma waves consistent with expectations of micro-instabilities associated with ion[14] and electron[16] velocity-space structure (Fig. 3). The electric field spectrum from about 11 kHz to about 1,688 kHz shows signatures of plasma quasi-thermal noise[37] (Fig. 3a) at the electron plasma frequency f_{pe} (which is used to estimate the total plasma density in Fig. 2a). Intense bursts of narrowband electrostatic Langmuir waves (Fig. 3a) occur throughout the perihelion encounter; narrowband Langmuir waves are driven by electron beams and damp rapidly, suggesting the presence of an intermittent, local population of electron beams.

The electric field spectrum (Fig. 3b) from 0.3 kHz to about 75 kHz shows intermittent bursts of electrostatic whistler-wave activity, peaked in power below the electron gyrofrequency f_{ce}. Also present are waves containing harmonic structure consistent with electron-Bernstein-wave emission. Electrostatic whistler–Bernstein bursts[16] are generated by features in the electron velocity distribution function $f_e(v)$ and are not observed in the solar wind at 1 AU. Here they occur only in the quiet radial-field intervals. A wavelet spectrogram (divided by a function $P_K \propto f^{-5/3}$) of the search coil magnetometer and fluxgate magnetometer data in Fig. 3c shows the spectral content of the magnetic field to around 146 Hz. A spectral break between 1–10 Hz (in the spacecraft frame) is highly variable and associated with the transition from a magnetohydrodynamic turbulent cascade to dissipation or dispersion ranges at ion kinetic lengthscales[38]. Note that the overall turbulent levels are lower and more intermittent in the quiet radial wind (Figs. 3c, 4a). The spectrum of magnetic helicity[39] σ_m in Fig. 3d indicates intervals of large ($1 > \sigma_m > 0.5$, red; $-0.5 < \sigma_m < -1$, blue) circular polarization often associated with ion cyclotron waves[40]. These ion wave events are apparent during quiet radial-field intervals.

The (trace) magnetic field spectra (see Methods), averaged over 30 min (Fig. 4a), show broken power-law behaviour, with spectral indices roughly comparable to the −5/3 and −8/3 predictions for magnetohydrodynamic and kinetic-scale turbulence[38], respectively. This suggests that by $36.6R_\odot$, the solar wind has already developed a turbulent cascade, to transport energy from large-scale motions to the microscale, where it can be dissipated. In the radial quiet wind (blue trace), where the turbulence level is substantially lower, an enhancement of wave power near the ion cyclotron frequency is observed. In the active jet wind (black trace), a steep spectrum is seen at the plasma ion inertial and gyroscales, indicating a transition to kinetic range turbulence and possibly the dissipation of turbulent energy to

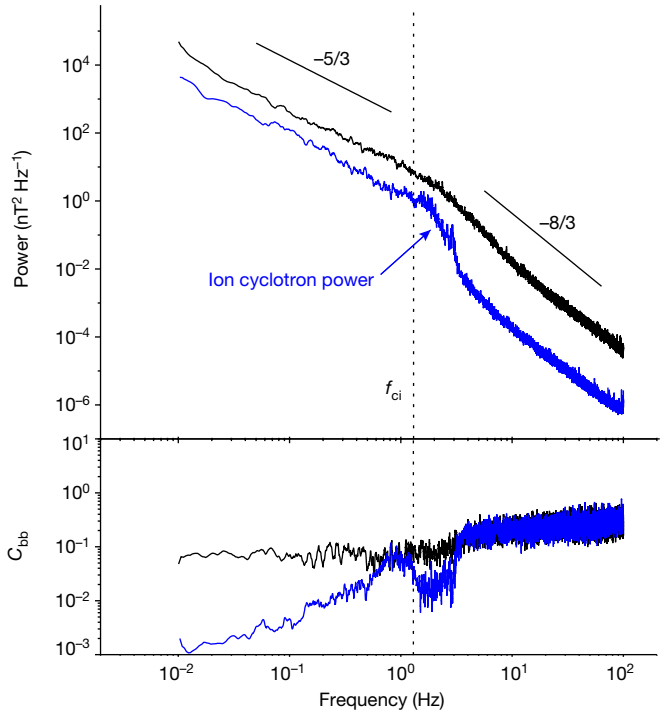

Fig. 4 | Power spectral density and magnetic compressibility of magnetic field fluctuations in quiet and jet wind. a, Thirty-minute integrated power spectra of fluctuations in quiet (blue) and jet (black) solar wind conditions show the transition from a magnetohydrodynamic inertial range to dissipation- or dispersion-range turbulence, here compared to the spacecraft-frame frequency $f^{-5/3}$ and $f^{-8/3}$ power laws. The quiet wind spectrum (blue) shows increased power near the ion cyclotron frequency (f_{ci}; dashed vertical line) that is associated with enhanced magnetic helicity (Fig. 3e). **b**, The ratio of magnitude (|**B**|) to tr(**B**) spectra indicates increased magnetic compressibility during jet intervals (black) compared to quiet wind (blue) up to the dissipation scale (a slope of −8/3). The ion cyclotron band corresponds to lower compressibility, as expected.

heat the solar wind as it expands to fill the heliosphere. In both types of wind, the power levels are several orders of magnitude larger than at 1 AU. The magnetic compressibility[41]—defined as $C_{bb} = (\delta|\mathbf{B}|/|\delta\mathbf{B}|)^2$—shows an increase at high frequencies, as expected for kinetic range turbulence (Fig. 4b). At low frequencies, the compressibility is larger in jet wind than in quiet wind, but remains small (C_{bb} less than about 0.1), indicating that jet fluctuations have an enhanced compressible component but are still predominantly Alfvénic[41]. In the quiet wind, the band of enhanced power near the cyclotron frequency has a reduced magnetic compressibility, as expected for quasi-parallel ion cyclotron waves[40].

PSP encounter 1 reveals a more structured and dynamic solar wind than is seen at 1 AU, with impulsive magnetic field reversals and plasma jets embedded in a quiet radial wind emerging from a small equatorial coronal hole. As PSP goes to lower altitudes, eventually to $9.8R_{\odot}$ during the upcoming solar maximum, we expect to descend below the the altitude where the wind becomes super-Alfvénic ($v_R > v_A$) and measure the interface between the corona and the solar wind for the first time.

Online content

Any methods, additional references, Nature Research reporting summaries, source data, extended data, supplementary information, acknowledgements, peer review information; details of author contributions and competing interests; and statements of data and code availability are available at https://doi.org/10.1038/s41586-019-1818-7.

1. Parker, E. N. Dynamics of the interplanetary gas and magnetic fields. *Astrophys. J.* **128**, 664–676 (1958).
2. Neugebauer, M. & Snyder, C. W. Solar plasma experiment. *Science* **138**, 1095–1097 (1962).
3. McComas, D. J. et al. Weaker solar wind from the polar coronal holes and the whole Sun. *Geophys. Res. Lett.* **35**, L18103 (2008).
4. Abbo, L. et al. Slow solar wind: observations and modeling. *Space Sci. Rev.* **201**, 55–108 (2016).
5. Lapenta, G. & Knoll, D. A. Effect of a converging flow at the streamer cusp on the genesis of the slow solar wind. *Astrophys. J.* **624**, 1049–1056 (2005).
6. Einaudi, G., Boncinelli, P., Dahlburg, R. B. & Karpen, J. T. Formation of the slow solar wind in a coronal streamer. *J. Geophys. Res.* **104**, 521–534 (1999).
7. Fisk, L. A. & Schwadron, N. A. The behavior of the open magnetic field of the Sun. *Astrophys. J.* **560**, 425–438 (2001).
8. Antiochos, S. K., Mikic, Z., Titov, V. S., Lionello, R. & Linker, J. A. A model for the sources of the slow solar wind. *Astrophys. J.* **731**, 112 (2011).
9. Wang, Y.-M. & Sheeley, N. R. On potential field models of the solar corona. *Astrophys. J.* **392**, 310–319 (1992).
10. Cranmer, S. R. Coronal holes. *Living Rev. Sol. Phys.* **6**, 3 (2009).
11. Hollweg, J. V. & Johnson, W. Transition region, corona, and solar wind in coronal holes: some two-fluid models. *J. Geophys. Res.* **93**, 9547–9554 (1988).
12. Verdini, A., Velli, M., Matthaeus, W. H., Oughton, S. & Dmitruk, P. A turbulence-driven model for heating and acceleration of the fast wind in coronal holes. *Astrophys. J. Lett.* **708**, 116–120 (2010).
13. Parker, E. N. Heating solar coronal holes. *Astrophys. J.* **372**, 719–727 (1991).
14. Cranmer, S. R., Field, G. B. & Kohl, J. L. Spectroscopic constraints on models of ion cyclotron resonance heating in the polar solar corona and high-speed solar wind. *Astrophys. J.* **518**, 937–947 (1999).
15. Fox, N. J. et al. The Solar Probe Plus mission: humanity's first visit to our star. *Space Sci. Rev.* **204**, 7–48 (2016).
16. Breneman, A. W. et al. STEREO and Wind observations of intense cyclotron harmonic waves at the Earth's bow shock and inside the magnetosheath. *J. Geophys. Res. Space Phys.* **118**, 7654–7664 (2013).
17. Bale, S. D. et al. The FIELDS instrument suite for Solar Probe Plus. *Space Sci. Rev.* **204**, 49–82 (2016).
18. Parker, E. N. Dynamical theory of the solar wind. *Space Sci. Rev.* **4**, 666–708 (1965).
19. Altschuler, M. D. & Newkirk, G. Magnetic fields and structure of the solar corona: 1. Methods of calculating coronal fields. *Sol. Phys.* **9**, 131–149 (1969).
20. Schatten, K. H., Wilcox, J. M. & Ness, N. F. A model of interplanetary and coronal magnetic fields. *Sol. Phys.* **6**, 442–455 (1969).
21. Arge, C. N. & Pizzo, V. J. Improvement in the prediction of solar wind conditions using near-real time solar magnetic field updates. *J. Geophys. Res. Space Phys.* **105**, 10465–10479 (2000).
22. Riley, P. et al. A comparison between global solar magnetohydrodynamic and potential field source surface model results. *Astrophys. J.* **653**, 1510–1516 (2006).
23. Hoeksema, J. T. *Structure and Evolution of the Large Scale Solar and Heliospheric Magnetic Fields*. PhD thesis, Stanford Univ. (1984).
24. Lee, C. O. et al. Coronal field opens at lower height during the solar cycles 22 and 23 minimum periods: IMF comparison suggests the source surface should be lowered. *Sol. Phys.* **269**, 367–388 (2011).
25. Riley, P. et al. Predicting the structure of the solar corona and inner heliosphere during Parker Solar Probe's first perihelion pass. *Astrophys. J. Lett.* **874**, 15 (2019).
26. Levine, R. H., Altschuler, M. D., Harvey, J. W. & Jackson, B. V. Open magnetic structures on the Sun. *Astrophys. J.* **215**, 636–651 (1977).
27. Kasper, J. C. et al. Solar Wind Electrons Alphas and Protons (SWEAP) investigation. *Space Sci. Rev.* **204**, 131 (2016).
28. McComas, D. J. et al. Probing the energetic particle environment near the Sun. *Nature* https://doi.org/10.1038/s41586-019-1811-1 (2019).
29. Belcher, J. W. & Davis, L. Large-amplitude Alfvén waves in the interplanetary medium, 2. *J. Geophys. Res.* **76**, 3534–3563 (1971).
30. Howes, G. G. et al. The slow mode nature of compressible wave power in solar wind turbulence. *Astrophys. J. Lett.* **753**, 19 (2012).
31. Horbury, T. S. et al. Short, large-amplitude speed enhancements in the near-Sun fast solar wind. *Mon. Not. R. Astron. Soc.* **478**, 1980–1986 (2018).
32. Gosling, J. T., Tian, H. & Phan, T. D. Pulsed Alfvén waves in the solar wind. *Astrophys. J. Lett.* **737**, 35 (2011).
33. Balogh, A., Forsyth, R. J., Lucek, E. A., Horbury, T. S. & Smith, E. J. Heliospheric magnetic field polarity inversions at high heliographic latitudes. *Geophys. Res. Lett.* **26**, 631–634 (1999).
34. Yamauchi, Y., Moore, R. L., Suess, S. T., Wang, H. & Sakurai, T. The magnetic structure of Hα macrospicules in solar coronal holes. *Astrophys. J.* **605**, 511–520 (2004).
35. Raouafi, N.-E. & Stenborg, G. Role of transients in the sustainability of solar coronal plumes. *Astrophys. J.* **787**, 118 (2014).
36. Roberts, M. A., Uritsky, V. M., DeVore, C. R. & Karpen, J. T. Simulated encounters of the Parker Solar Probe with a coronal-hole jet. *Astrophys. J.* **866**, 14 (2018).
37. Meyer-Vernet, N., Issautier, K. & Moncuquet, M. Quasi-thermal noise spectroscopy: the art and the practice. *J. Geophys. Res. Space Phys.* **122**, 7925–7945 (2017).
38. Schekochihin, A. A. et al. Astrophysical gyrokinetics: kinetic and fluid turbulent cascades in magnetized weakly collisional plasmas. *Astrophys. J.* **182**, 310–377 (2009).
39. Matthaeus, W. H., Goldstein, M. L. & Smith, C. Evaluation of magnetic helicity in homogeneous turbulence. *Phys. Rev. Lett.* **48**, 1256–1259 (1982).
40. Jian, L. K. et al. Electromagnetic waves near the proton cyclotron frequency: STEREO observations. *Astrophys. J.* **786**, 123 (2014); erratum **847**, 1 (2017).
41. Bruno, R. & Carbone, V. The solar wind as a turbulence laboratory. *Living Rev. Sol. Phys.* **10**, 2 (2013).

[1]Space Sciences Laboratory, University of California, Berkeley, CA, USA. [2]Physics Department, University of California, Berkeley, CA, USA. [3]The Blackett Laboratory, Imperial College London, London, UK. [4]School of Physics and Astronomy, Queen Mary University of London, London, UK. [5]Smithsonian Astrophysical Observatory, Cambridge, MA, USA. [6]School of Physics and Astronomy, University of Minnesota, Minneapolis, MN, USA. [7]Department of Physics & Astronomy, University of New Hampshire, Durham, NH, USA. [8]Space Science Center, University of New Hampshire, Durham, NH, USA. [9]Department of Physics, University of Maryland, College Park, MD, USA. [10]Institute for Physical Science and Technology, University of Maryland, College Park, MD, USA. [11]Joint Space Science Institute, University of Maryland, College Park, MD, USA. [12]LPC2E, University of Orléans, CNRS, Orléans, France. [13]Laboratory for Atmospheric and Space Physics, University of Colorado, Boulder, CO, USA. [14]Code 695, NASA Goddard Space Flight Center, Greenbelt, MD, USA. [15]Goddard Planetary Heliophysics Institute, University of Maryland Baltimore County, Baltimore, MD, USA. [16]Code 672, NASA Goddard Space Flight Center, Greenbelt, MD, USA. [17]Department of Physics and Astronomy, University of Iowa, Iowa City, IA, USA. [18]Climate and Space Sciences and Engineering, University of Michigan, Ann Arbor, MI, USA. [19]Heliophysics Division, NASA Goddard Space Flight Center, Greenbelt, MD, USA. [20]University of Applied Sciences and Arts Northwestern Switzerland, Windisch, Switzerland. [21]LESIA, Observatoire de Paris, Université PSL, Sorbonne Université, CNRS, Meudon, France. [22]Department of Astrophysical Sciences, Princeton University, Princeton, NJ, USA. [23]Johns Hopkins University Applied Physics Laboratory, Laurel, MD, USA. [24]Department of Earth, Planetary, and Space Sciences, University of California, Los Angeles, CA, USA. *e-mail: bale@berkeley.edu

Methods

Heliocentric RTN coordinates

We use so-called heliocentric RTN coordinates in our study. R points from the Sun centre to the spacecraft. T lies in the spacecraft plane (close to the ecliptic) and is defined as the cross product of the solar rotation axis with R. T points in the direction of prograde rotation. N completes a right-handed system.

Statistical modes

To examine the large-scale magnetic structure (Fig. 1b), we seek to remove the rapidly varying spikes observed in Fig. 1a. To do this we produce statistical modes which are defined by binning the full cadence magnetic field observations into one-hour intervals and for each interval, calculating the modal value—the peak of the histogram of field values within each interval.

Identification of jet intervals

We calculate that approximately 6% of the duration of encounter 1 consists of jet intervals. That number is computed by measuring the duration of positive polarity B_R intervals (58,973 s) occurring from 30 October 2018 to 11 November 2018 UT (103,6800 s total). This interval was chosen to correspond to the negative polarity interval centred on D (Fig. 1b), which has primarily negative polarity over the coronal hole, and does not have transient coronal mass ejection events. The positive-polarity jets were identified using a simple zero-crossing algorithm applied to 1-s cadence radial magnetic field data B_R. Of course, not all so-called jets contain full polarity reversals. Biasing this calculation with an amplitude offset will produce a larger fraction of jet times; this is an ongoing study.

PSP/FIELDS measurement details

Measurements presented here were made by the FIELDS[17] and SWEAP[27] instruments on the PSP spacecraft. Magnetic field measurements in Fig. 1a were made by the FIELDS fluxgate magnetometer and are averaged to 1-s cadence from their native cadence, which varies from about 2.3 to 293 samples per second over encounter 1. The B_R data shown in Fig. 1b are derived from the 1-s data by computing the distribution of amplitudes in one-hour intervals with an amplitude resolution of 1 nT, and by finding the peak value of that distribution: that is, the statistical mode. This technique removes the fluctuating 'jet' intervals, without introducing the amplitude bias of an averaging algorithm.

The magnetic field measurements in Fig. 2 start at 1-s cadence, averaged down from their native cadence as described above. All magnetic field measurements here are calibrated accurate to better than 0.5 nT. SWEAP velocity measurements are made by the Solar Probe Cup (SPC) sensor at a cadence of about 1 measurement per 0.87 s and then averaged to 5-s intervals. The 1-s cadence magnetic field data are then averaged onto these 5-s time intervals. This reduces fluctuation noise in the SPC data and provides velocity and magnetic field measurements at the same cadence. The plasma density measurements in Fig. 1a are made using the FIELDS Low Frequency Receiver (LFR)[42], which measures the fluctuating electric field across the V1-V2 antenna pair[17] and computes the spectral density (also shown in Fig. 3a). The spectral peak is identified and associated with the electron plasma frequency f_{pe}, as described previously[37]. Hence, the frequency of the peak amplitude gives a reliable estimate of the total plasma density. The spectral resolution of the LFR instrument is $\Delta f/f \approx 4\%$. The plasma frequency f_{pe} is proportional to $\sqrt{n_e}$, where n_e is the electron (total) density; therefore the resulting uncertainty in the density measurement is $\Delta n/n \approx 2\Delta f/f \approx 8\%$. Electric field measurements used to compute the radial Poynting flux in Fig. 2b are measured directly as differential voltage pairs[43] between the V1-V2 and V3-V4 antennas[17] and are then calibrated to electric field units by comparison to $-\mathbf{v}\times\mathbf{B}$ as computed from the SPC velocity and fluxgate magnetometer data. This enables us to remove spacecraft offset electric fields and compute an effective probe-separation length, a standard technique used to calibrate electric field instrumentation[44]. The electric field measurement is accurate to approximately 1 mV m^{-1}.

Measurements in Fig. 3a show the full spectrum of the RFS/LFR[42] receiver in spectrogram form, as measured by the V1-V2 antenna pair. Wave intensity in Fig. 3a ranges from about 6×10^{-17} to 1.4×10^{-10} V^2 Hz^{-1} and is represented logarithmically. The spectral bandwidth of the LFR receiver is $\Delta f/f = 4.5\%$ and the cadence of the measurement is 1 spectrum per 7 s. Figure 3b shows the electric field spectrogram of differential voltage measurements on the V1-V2 antenna pair from the Digital Fields Board (DFB) subsystem[43], with intensity in arbitrary logarithmic amplitude units. The spectral resolution of this channel of the DFB is $\Delta f/f \approx$ ~6–12% and the measurement cadence is 1 spectrum per 5.5 s. Figure 3c shows the magnetic field spectrogram of search coil magnetometer measurements from DFB[43], with intensity in arbitrary logarithmic amplitude units. The wavelet spectrogram in Fig. 3d and magnetic helicity spectrum in Fig. 3e were computed using the *wav_data* routine for the IDL programming language in the SPEDAS[45] suite of IDL analysis routines. Wave intensity in Fig. 3c is represented in logarithmic power in arbitrary units and is divided by a factor $P_K \propto f^{-5/3}$ (flattened), such that a power spectrum with spectral index −5/3 has no frequency dependence.

PFSS modelling and connection to PSP

Modelling the magnetic field time series (Fig. 1b) and tracing field lines from PSP down into the corona (Fig. 1c, d) was performed in two main steps.

(1) PFSS implementation. PFSS[9,19,20] modelling used the recent open-source Python implementation *pfsspy*[46,47]. This code package is freely available online, extremely flexible with regard to changing the input parameters and efficient (a full PFSS solution can be extracted in about 14 s including downloading the magnetogram on demand). Given a magnetogram and source-surface radius (R_{SS}) as boundary conditions, the code solves the Laplace equation (equation (1)) for the magnetic scalar potential, Φ_B, and outputs a full three-dimensional magnetic field within the annular volume bounded by the photosphere and the source-surface parameter. The choice of magnetogram data and values of source-surface height depicted in Fig. 1 are discussed in Methods section 'Choice of magnetogram data and source-surface radius for Fig. 1' below.

$$\nabla^2\Phi_B(r) = 0 \tag{1}$$

(2) Ballistic propagation. The procedure to magnetically connect PSP to a particular location at the outer boundary of the PFSS solution domain follows refs. [48–50], where the field line intersecting the position of PSP is assumed to follow a Parker spiral[1] with a curvature determined by the co-temporal solar wind velocity measurement at that position. As discussed in ref. [48], although at lower radii this approximation is strongly perturbed by both corotational effects and the acceleration of the solar wind, these effects actually shift the coronal longitude by a similar magnitude but in opposite directions, resulting in an estimated error in longitude of less than 10°. This produces a very simple mapping (equation (2)) from spacecraft spherical Carrington coordinates (r_{PSP}, θ_{PSP}, ϕ_{PSP}) to coordinates on the source surface (r, θ, φ), involving the solar sidereal rotation rate, Ω_S, the measured solar wind speed, v_R, and the source-surface height R_{SS}.

$$\begin{pmatrix} r \\ \theta \\ \phi \end{pmatrix} = \begin{pmatrix} R_{SS} \\ \theta_{PSP} \\ \phi_{PSP} + \dfrac{\Omega_S}{v_R}(r_{PSP} - R_{SS}) \end{pmatrix} \tag{2}$$

To generate time series predictions, we first download a magnetogram, choose a source-surface height and generate a PFSS solution using equation (1). We then take the trajectory of PSP and use equation (2) to produce a time series of latitudes and longitudes on the source surface to which PSP was connected (see red and blue trajectories in Fig. 1c, d, Extended Data Figs. 1–3). For each latitude and longitude we obtain a B_R value at the source surface from the PFSS model. Finally, we scale each B_R value by $C(R_{SS}/r_{PSP})^2$ to produce an estimate of B_R at the location of PSP as a function of time. C is an empirically determined constant used to scale the time series prediction to match the peak measured magnetic field. Its value is dependent on the choice of magnetogram but approaches unity as the source-surface radius decreases and more flux is opened to the heliosphere. For the model results shown in Fig. 1, the values of C are 6.7 ($2.0R_\odot$ model) and 1.4 ($1.2R_\odot$ model).

To produce field line traces and generate Fig. 1c, d, we start with the time series of latitudes and longitudes on the source surface connected to PSP. For each pair of coordinates, we use *pfsspy*'s built-in field line tracer. Given the output of the *pfsspy* model, we supply the source-surface latitudes and longitudes and the field line tracer generates a field line which starts from that point and propagates it down to the photosphere. The model also provides a polarity for each field line generated, and we use these to colourize the field lines plotted in Fig. 1c, d.

Choice of magnetogram data and source-surface radius for Fig. 1

Synoptic maps of the photospheric magnetic field are available from multiple sources, which give variable outputs from the PFSS model. In this work we consider the NSO/GONG zero-point-corrected data product[51], SDO/HMI vector magnetogram data product[52], and the DeRosa (LMSAL) modelled magnetogram[53]. GONG has the advantage of being operationally certified for space weather predictions, SDO/HMI is space-based and offers better resolution, and the DeRosa model assimilates HMI data and uses a surface flux transport and far-side helioseismological data to simulate photospheric dynamics such as differential rotation.

Additional variation in the outputs of the PFSS model arises from the time evolution of photospheric observations. Synoptic magnetograms are built by many observations of the Sun from Earth as it rotates with an approximate 27-day period. Typically, only ±60° longitude about the central meridian (sub-Earth point) are used for each observation (the grey regions in Extended Data Figs. 1–3). Although these maps can be updated with new data as frequently as observations are made, parts of the Sun facing away from Earth cannot be updated until they rotate into view, meaning all synoptic maps consist of a mix of old and new data and evolve in time.

Finally, the model output depends considerably on the choice of the source-surface radius parameter (R_{SS}). The inferred structure at the source surface changes as the source surface is lowered; implied structure such as the PIL—the contour of $B_R = 0$—becomes more structured and warped. The foot points of open field lines at the photosphere encompass larger areas, increasing the predicted size of coronal holes, and also increasing the total amount (both positive and negative) of magnetic flux crossing the source surface.

Our approach to make robust conclusions is to generate model results for multiple times from all three magnetogram sources for varying source surface radii. Colour maps of B_R at the source surface and the associated PILs are shown in Extended Data Figs. 1–3. The majority of models at $2.0R_\odot$ and below predict polarity inversions in the vicinity of 240° and 310° longitude at all source-surface radii, with additional polarity inversions around 10° and 140° longitude that develop at lower source-surface radii. These features are all consistent with PSP measurements; we emphasize that they are largely independent of the time of observation and the choice of magnetogram source. Although the established[23] value of $2.5R_\odot$ still gives good results from a GONG evaluation, both the HMI and DeRosa models produce strong disagreement around the time of perihelion. In Fig. 1b–d we show results from the GONG zero-point-corrected map evaluated on 6 November 2018 UT about which our time range of analysis is symmetric. This evaluation shows all the above features and produces good time series agreements. We show source-surface radii of $2.0R_\odot$ and $1.2R_\odot$. These lower source-surface radii do have modern precedent: $2.0R_\odot$ is consistent with previous PFSS modelling done for the same interval[25], where that radius was chosen to better match the observed extent of coronal holes. Another previous work[24] investigated the impact of lowering the source surface radius on model results, observing that at solar minimum a lower ($<2.0R_\odot$) source-surface radius was required to populate equatorial coronal holes with open field lines and improve their estimates of magnetic field strength at 1 AU.

Data availability

The data used in this study are available at the NASA Space Physics Data Facility (SPDF), https://spdf.gsfc.nasa.gov/index.html.

42. Pulupa, M. et al. The Solar Probe Plus Radio Frequency Spectrometer: measurement requirements, analog design, and digital signal processing. *J. Geophys. Res. Space Phys.* **122**, 2836–2854 (2017).
43. Malaspina, D. M. et al. The Digital Fields Board for the FIELDS instrument suite on the Solar Probe Plus mission: analog and digital signal processing. *J. Geophys. Res. Space Phys.* **121**, 5088–5096 (2016).
44. Mozer, F. S. DC and low-frequency double probe electric field measurements in space. *J. Geophys. Res. Space Phys.* **121**, 10942–10953 (2016).
45. Angelopoulos, V. et al. The Space Physics Environment Data Analysis System (SPEDAS). *Space Sci. Rev.* **215**, 9 (2019).
46. Stansby, D. Dstansby/pfsspy: *pfsspy* 0.1.2 https://zenodo.org/record/3237053#.Xcqc-1f7SUk (2019).
47. Yeates, A. Antyeates1983/pfss: first release of pfss code https://zenodo.org/record/1472183#.XcqdU1f7SUk (2018).
48. Nolte, J. T. & Roelof, E. C. Large-scale structure of the interplanetary medium. I: High coronal source longitude of the quiet-time solar wind. *Sol. Phys.* **33**, 241–257 (1973).
49. Neugebauer, M., et al. Spatial structure of the solar wind and comparisons with solar data and models. *J. Geophys. Res.* **103**, 14587–14599 (1998).
50. Stansby, D., Horbury, T. S., Wallace, S. & Arge, C. N. Predicting large-scale coronal structure for Parker Solar Probe using open source software. *RNAAS* **3**, 57 (2019).
51. Clark, R., Harvey, J., Hill, F. & Toner, C. GONG magnetogram zero-point-correction status. *Bull. Am. Astron. Soc.* **35**, 822 (2003).
52. Hoeksema, J. T. et al. The Helioseismic and Magnetic Imager (HMI) vector magnetic field pipeline: overview and performance. *Sol. Phys.* **289**, 3483–3530 (2014).
53. Schrijver, C. J. & DeRosa, M. L. Photospheric and heliospheric magnetic fields. *Sol. Phys.* **212**, 165 (2003).

Acknowledgements The FIELDS experiment on the Parker Solar Probe spacecraft was designed and developed under NASA contract NNN06AA01C. The FIELDS team acknowledges the contributions of the Parker Solar Probe mission operations and spacecraft engineering teams at the Johns Hopkins University Applied Physics Laboratory. S.D.B. acknowledges the support of the Leverhulme Trust Visiting Professorship programme. Contributions from S.T.B. were supported by NASA Headquarters under the NASA Earth and Space Science Fellowship Program grant 80NSSC18K1201. This work uses data obtained by the Global Oscillation Network Group (GONG) programme, managed by the National Solar Observatory, which is operated by AURA, Inc. under a cooperative agreement with the National Science Foundation. The data were acquired by instruments operated by the Big Bear Solar Observatory, High Altitude Observatory, Learmonth Solar Observatory, Udaipur Solar Observatory, Instituto de Astrofísica de Canarias and Cerro Tololo Interamerican Observatory. D.B. was supported by UK STFC grant ST/P000622/1. J.P.E. and T.S.H. were supported by UK STFC grant ST/S000364/1. D.S. was supported by UK STFC grant ST/N000692/1. C.H.K.C. is supported by STFC Ernest Rutherford Fellowship number ST/N003748/2. T.D.d.W. and V.V.K. are supported by CNES.

Author contributions S.D.B. wrote the manuscript with substantial contributions from S.T.B., B.D.G.C., C.H.K.C., T.S.H., M. Maksimovic, T.D.P. and M.V. All authors participated in the data interpretation, and read and commented upon the manuscript. S.D.B. led the FIELDS instrument team with contributions from J.W.B., T.A.B, T.D.d.W., K.G., P.R.H., D.E.L., R.J.M., M. Maksimovic, D.M.M., M.P. and N.E.R.

Competing interests The authors declare no competing interests.

Additional information

Correspondence and requests for materials should be addressed to S.D.B.

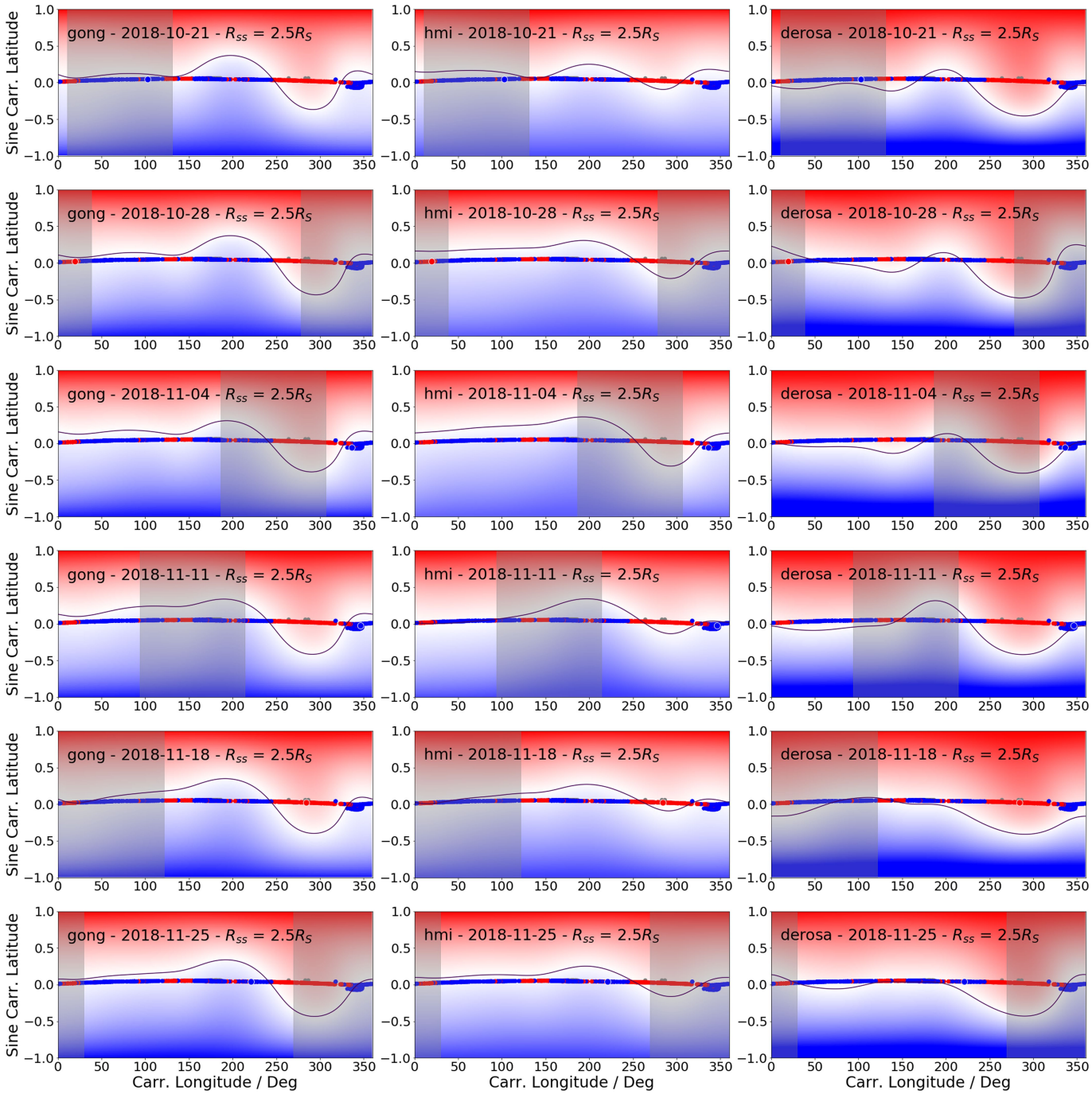

Extended Data Fig. 1 | Variation of PFSS neutral line topology with time and magnetogram choice at $R_{ss} = 2.5R_{\odot}$. Colour maps of B_R at the source surface from PFSS extractions with source-surface radius $R_{SS} = 2.5R_{\odot}$. Red indicates positive polarity and blue indicates negative polarity. The black line shows the PIL (the contour of $B_R = 0$). Superposed is the ballistically projected PSP trajectory coloured by the measured polarity. Perihelion occurred around 330° longitude. Left to right, the columns show extractions from the NSO/GONG, SDO/HMI and DeRosa LMSAL models. From top to bottom, the models are evaluated at a weekly cadence spanning six weeks about perihelion, with input magnetograms from each source taken as close in time as possible. The grey shading shows the region ±60° about the central meridian on the date of the model evaluation, indicating the portion of the Sun that could be observed at the time of observation.

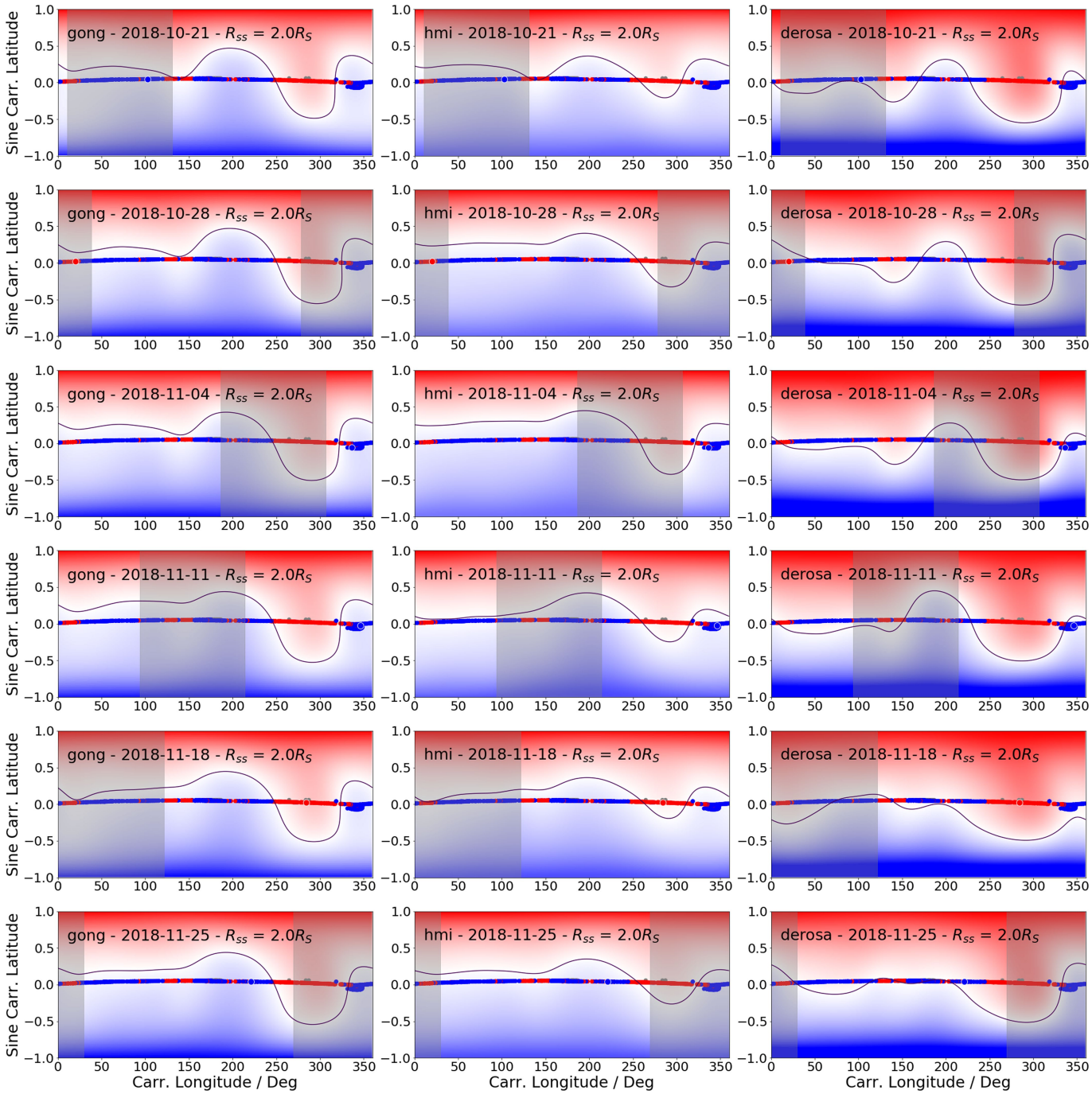

Extended Data Fig. 2 | Variation of PFSS neutral line topology with time and magnetogram choice at R_{ss} = 2.0$R_\odot$. Colour maps of B_R at the source surface from PFSS extractions with R_{SS} = 2.0$R_\odot$. Other features are as described in Extended Data Fig. 1.

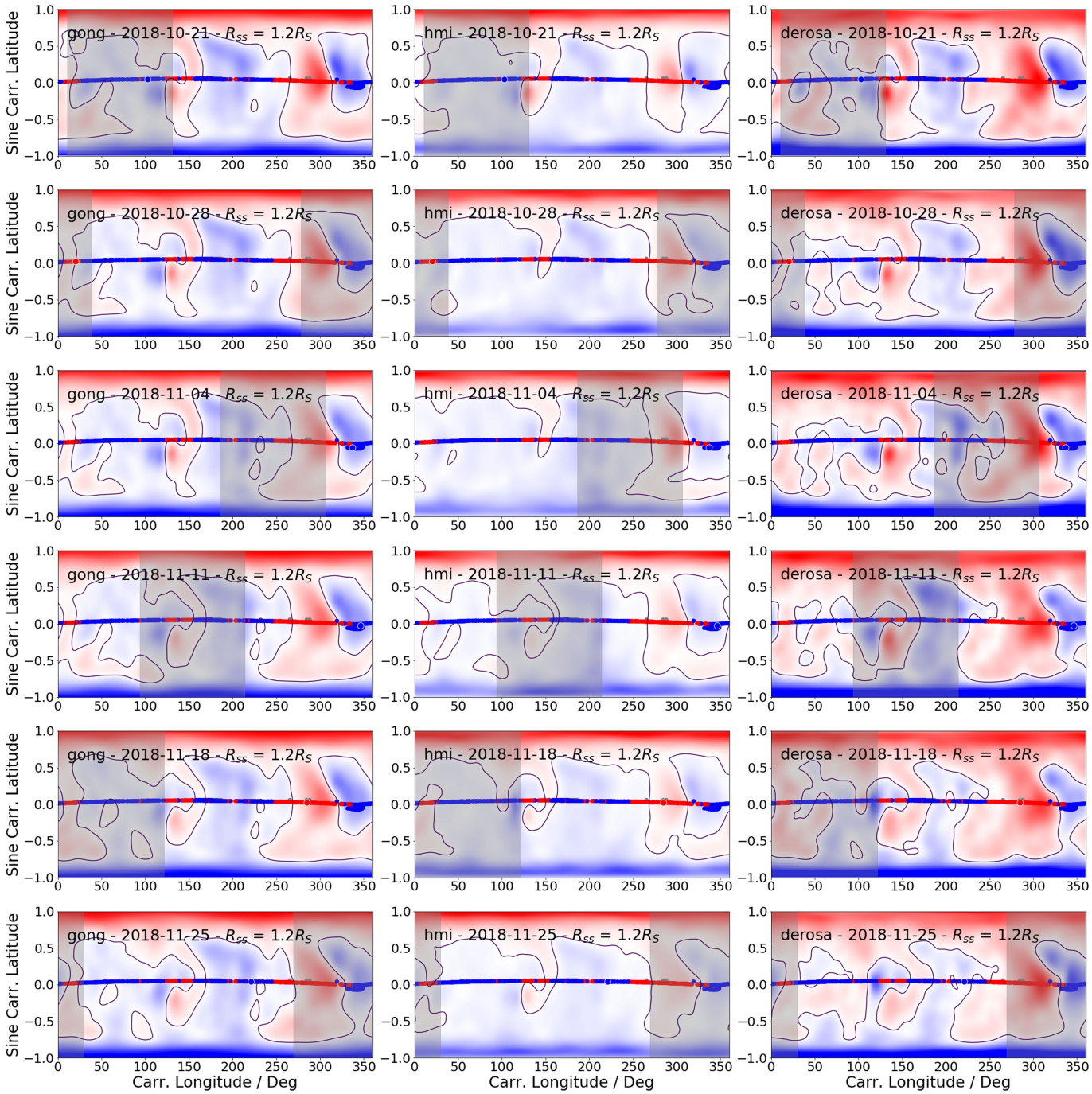

Extended Data Fig. 3 | Variation of PFSS Neutral Line topology with time and magnetogram choice at R_{ss} = 1.2$R_\odot$. Colour maps of B_R at the source surface from PFSS extractions with R_{SS} = 1.2$R_\odot$. Other features are as described in Extended Data Fig. 1.

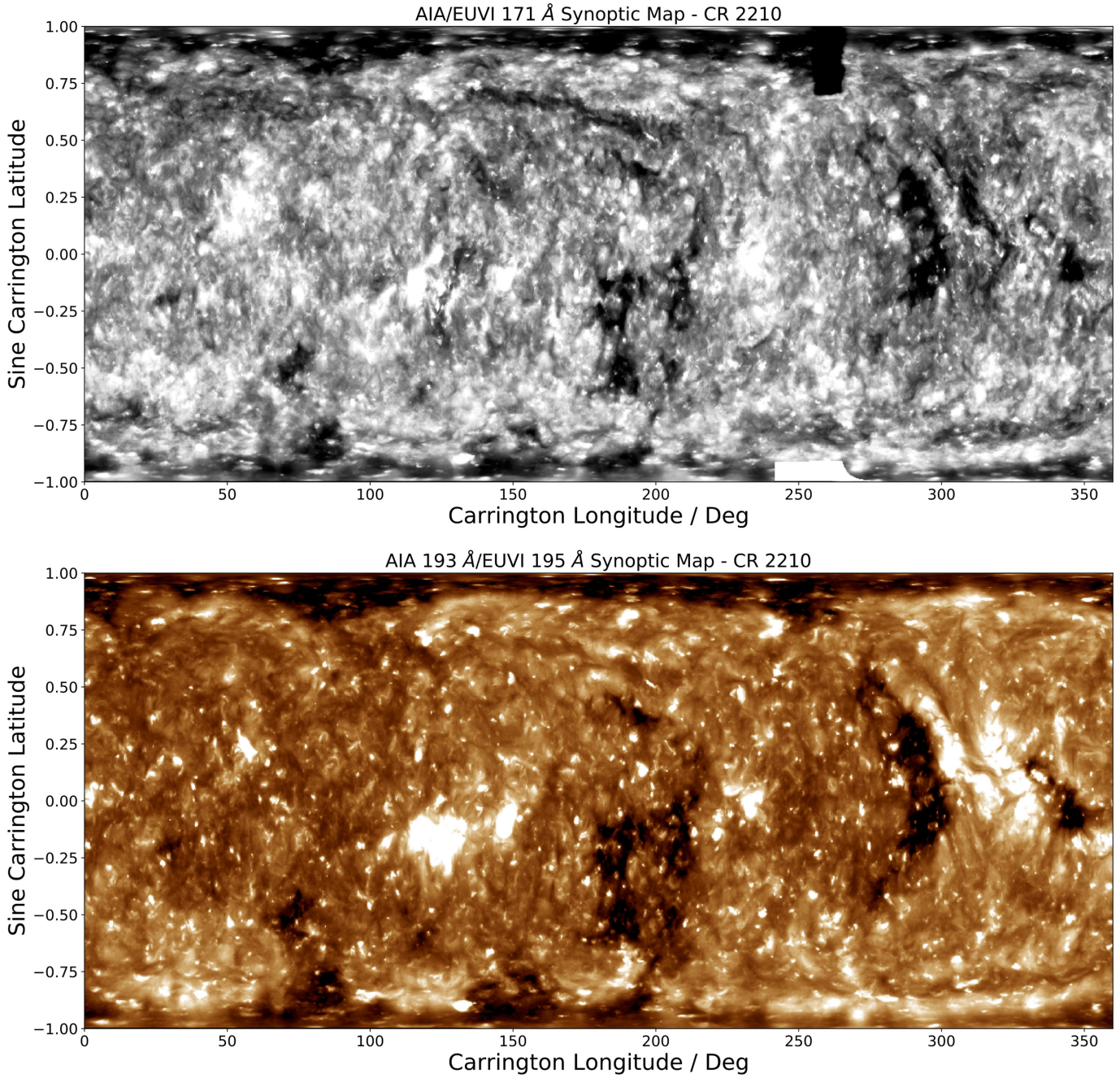

Extended Data Fig. 4 | Synoptic maps of extreme-ultraviolet coronal emission from Carrington rotation 2,210, assembled from the STEREO-A/EUVI and SDO/AIA instruments. Top, 171-Å data showing coronal Fe IX emission at around 600,000 K. This is the background of Fig. 1c, d. Bottom, 193-Å (AIA) and 195-Å (EUVI) data showing emission from coronal Fe XII emission at around 1,000,000 K. The brightness is positively correlated with the integrated plasma density squared along the line of sight. The dark regions in both images are probable locations of coronal holes, which are threaded by open magnetic field lines that allow plasma to evacuate into interplanetary space, resulting in under-dense regions. Carrington rotation 2,210 occurred from 20:51 26 October 2018 UT to 04:11 23 November 2018 UT.

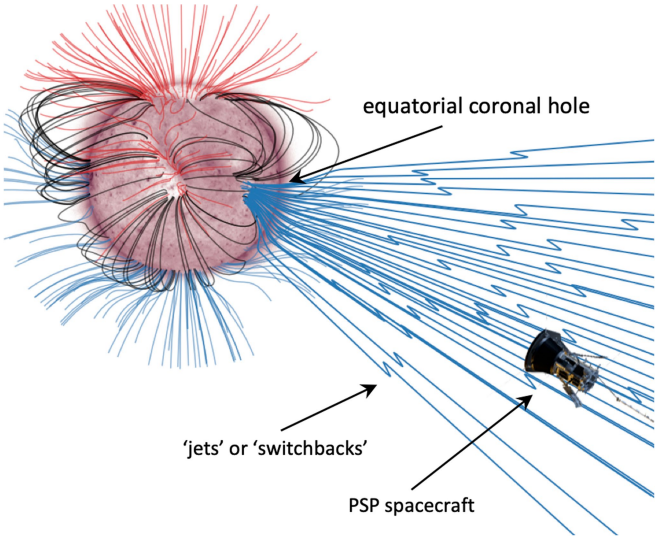

Extended Data Fig. 5 | During encounter 1, PSP connected magnetically to a small negative-polarity equatorial coronal hole. This schematic shows a potential field extrapolation of the solar magnetic field at the time of the first perihelion pass of PSP. The solar surface is shown, coloured by AIA 211-Å extreme-ultraviolet emission (see Extended Data Fig. 4 for other wavelengths). Coronal holes appear as a lighter shade. Superposed are various field lines initialized at the solar disk. Black lines indicate closed loops, blue and red illustrate open field lines with negative and positive polarities, respectively. As depicted here and in Fig. 1c, d, at perihelion PSP connected to a negative equatorial coronal hole. The 'switchbacks' (the jets) observed by PSP (Fig. 1a) are illustrated as kinks in the open field lines emerging from the coronal hole that connect to PSP. (Note that neither the radial distance to the spacecraft nor the scale or amplitude of the jets or switchbacks are to scale.) Spacecraft graphic is courtesy of NASA/Johns Hopkins APL.